Journal of
Ceramic Science
and Technology

J. Ceram. Sci. Tech., 07 [03] 249-256 (2016)
DOI: 10.4416/JCST2015-00085
available online at: http://www.ceramic-science.com

Sintering of Magnesia and Iron Oxide in Air and Flowing Nitrogen and its Corrosion Process by Molten Electrolyte

Y.B. Xu, Y.W. Li*, J.H. Yang, S.B. Sang, Q.W. Qin

The State Key Laboratory of Refractories and Metallurgy, Wuhan University of Science and Technology, 430081 Wuhan, PR China

received December 9, 2015; received in revised form January 25, 2016; accepted February 10, 2016

Abstract

In the present paper, novel sidewall materials for aluminum reduction cells were prepared in air and nitrogen using magnesia and magnetite powders. The sintering behavior of the specimens and their corrosion resistance to electrolyte have been investigated. The results show that Fe_3O_4 phase is transformed into Fe_2O_3 at high temperatures in air, which in turn reacts with the MgO added to form $MgFe_2O_4$. For the specimens prepared in nitrogen, most of the Fe_3O_4 is reduced to FeO in specimens without MgO while all the specimens with added MgO are composed of $Fe_xMg_{1-x}O$ only. The densification of the specimens prepared in both air and nitrogen decreased with the MgO content. The corrosion tests showed that corrosion layers were produced in all the MgO-added specimens while the corrosion process was inhibited in case of formation of composite spinel layer on the surface of the specimens during the tests. Moreover, since $MgFe_2O_4$ exhibits higher chemical stability than that of $Fe_xMg_{1-x}O$ in electrolyte and a protective composite spinel layer with dense structure can be more easily formed in specimens prepared in air, the specimens prepared in air generally exhibited better corrosion resistance than that of the specimens prepared in nitrogen. The corrosion processes were also analyzed and discussed based on thermodynamic calculations.

Keywords: Sidewalls, MgO-Fe_2O_3(FeO), composite spinel, electrolyte, corrosion resistance

I. Introduction

Aluminium is commercially produced in aluminium reduction cells. The overall cell life is largely determined by the service life of the sidewalls [1]. Si_3N_4-bonded SiC materials have been widely utilized as sidewalls because of their excellent properties, such as high hardness, good thermal shock resistance and high thermal conductivity [2–5]. Rapid heat dissipation through the sidewalls owing to their high thermal conductivity leads to the formation of solidified electrolyte, normally referred to as a side ledge, on the sidewalls, which protects the sidewalls from corrosive electrolyte melt and hence greatly extends the service life of the sidewalls. However, to maintain the side ledge, a large amount of heat, accounting for approximately 35 % of the total input energy, has to be transferred [6], which is the reason for the low energy efficiency of 40–45 % in the current aluminum electrolysis process. This heat dissipation should be minimized in order to meet the energy-saving requirements currently faced by the aluminum industries [7]. To conserve the heat in the cell, a high insulation layer could be applied outside the sidewalls. In this case, however, the sidewalls would be in direct contact with oxidizing gas, corrosive electrolyte and molten aluminum from the top to the bottom since the frozen ledge would no longer be existent. And the lifetime of the Si_3N_4-bonded SiC materials would be reduced significantly as a result of the attack by the corrosive electrolyte together with oxidizing gas [8]. Therefore, new types of sidewall materials with high resistance to oxidation and electrolyte are required for gas and bath zones within a ledge-free cell.

In a ledge-free cell, the service environment of the sidewalls at the gas and bath zones is the same as that of the anode materials [7]. $NiFe_2O_4$ spinel ceramic has been considered as the most promising inert anode owing to its high stability in air and molten electrolyte [9–11]. It is therefore of interest as a novel sideling materialas well [7, 12, 13]. However, the low rate of finished products of $NiFe_2O_4$ ceramics and their high manufacturing costs owing to the scarcity of Ni resources eliminate the possibility for the wide use of such material as sidewalls [14].

Besides $NiFe_2O_4$, some other spinels, such as $FeAl_2O_4$, $MgAl_2O_4$ and $NiAl_2O_4$, also exhibit high chemical stability in electrolyte melts [1, 15, 16]. And the stability of composite spinel formed by solid solution reaction of various spinels tends to improve further. For example, in some cases the $Ni_{0.4}Mg_{0.6}Fe_2O_4$ composite spinel exhibits even better corrosion resistance to electrolyte than the pure $NiFe_2O_4$ spinel [17]. And $(Ni,Mg)Al_2O_4$ also attains better chemical stability in electrolyte than $NiAl_2O_4$ and $MgAl_2O_4$ [1]. Correspondingly, when they tested the corrosion resistance of nickel ferrite in a cryolite-based bath, Olsen and Thonstad [16] observed that the presence of a $NiFe_2O_4$-$FeAl_2O_4$-$NiAl_2O_4$ composite spinel layer on the surface of the specimen effectively hindered the attack of electrolyte. Similarly, in our previous

* Corresponding author: liyawei@wust.edu.cn

work [18], we assessed the corrosion resistance of MgO-$NiFe_2O_4$-TiO_2 material to electrolyte and found that the $Ni(Fe,Al)_2O_4$ dense composite spinel layerformed on the specimens during the test further improved the corrosion resistance of the material.

In fact, MgO-Fe_2O_3(FeO) materials may be a candidate to replace Si_3N_4-bonded SiC refractories in the gas and bath zones. Firstly, the MgO-Fe_2O_3(FeO) materials prepared by means of substitution of MgO for NiO in the NiO-Fe_2O_3 material system can effectively lower the manufacturing costs of the sidewalls and reduce the risk of aluminum contamination. Secondly, spinel phases such as $MgFe_2O_4$ and $(Mg,Fe)Fe_2O_4$ would form in the MgO-Fe_2O_3(FeO) materials [19,20], which would probably endow the materials with high chemical stability in the electrolyte. Meanwhile, during the corrosion process, the reaction product Al_2O_3 would react with the materials to generate a composite spinel layer on the surface of the materials, which might effectively prevent the materials from further attack by the corrosive electrolyte.

The present work aims to develop a ledge-free sidewall material for gas and bath zones using light magnesia and magnetite as starting materials. Sintering atmospheres of air and nitrogen were adopted to adjust the transformation of Fe_3O_4 to other ferrites (such as FeO, Fe_2O_3) [21]. Firstly, the phase evolutions and sintering behavior of the selected mixtures are studied at high temperatures. Subsequently, the corrosion resistance of the specimens is evaluated in molten electrolyte (AlF_3-Na_3AlF_6-K_3AlF_6) in air at 900 °C. Finally, the electrolyte corrosion mechanism is proposed, taking into account the results of thermodynamic calculations.

II. Experimental

(1) Specimen preparation

In this experiment, light magnesia powder (D_0 = 3.579 μm, 98.5 wt% MgO, Sinopharm Chemical Reagent Co., Ltd., Shanghai, China) and magnetite (D_0 =3.759 μm, 99 wt% Fe_3O_4, Aladdin Industrial Corporation, Shanghai, China) were used as raw materials. Five groups of specimens were designed with the batch compositions presented in Table 1. All raw materials were mixed for 120 min in a ball mill at the rotating speed of 90 – 110 rpm, and then the mixed powders were pressed to form cylindrical specimens measuring 20 mm in diameter and 20 mm in height under a pressure of 120 MPa. All the specimens were fired in an electric furnace at 1400 °C for a soaking time of 3 h in air and nitrogen (99.999 % N_2), the heating rate was 4 °C/min. After firing, the furnace was allowed to cool to room temperature. The specimens prepared in air and nitrogen were labeled M0, M5, M10, M20, M30 and NM0, NM5, NM10, NM20, NM30, respectively. The phase equilibrium diagram predicted (Fig. 1) suggests that Fe_3O_4 probably transforms to Fe_2O_3 and FeO respectively after firing at 1400 °C in air and nitrogen.

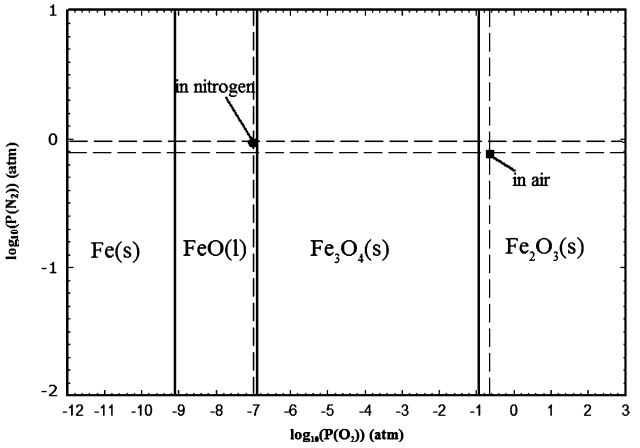

Fig. 1: Phase equilibrium diagram of Fe-N-O system at 1400 °C (FactSage version 6.2).

(2) Characterization

The bulk density and true density of the fired specimens were determined based on the Archimedes principle and with an automatic true density meter (AccuPyc 1330, Micromeritics, USA). The phase composition of the specimens before and after the corrosion test was analysed by means of X-ray diffraction (XRD, X'pert Pro, Philips, using Ni-filtered, Cu Ka radiation at scanning speed of 2 deg/min at a temperature of 16 °C) using powders from the milled specimens under 325 mesh sieve. The microstructures of the specimens were observed with a scanning electron microscope (SEM, Quanta 400, FEI Company, USA) linked with an energy-dispersive spectroscopy (EDS, EDAX, Phoenix) system.

The corrosion test for the specimens was conducted by immersing the specimens in a premixed Na_3AlF_6-AlF_3-K_3AlF_6 electrolyte contained in stainless steel crucibles with lids. The crucibles were heated to 900 °C and held at this temperature for 10 h in an electric furnace with an air atmosphere outside the crucibles. The chemical composition of the premixed Na_3AlF_6-AlF_3-K_3AlF_6 electrolyte bath was $57.8K_3AlF_6$-$16.7Na_3AlF_6$-$25.5AlF_3$ (wt%) (AlF_3, Na_3AlF_6 and K_3AlF_6, reagent grade, Sinopharm Chemical Reagent Co., Ltd., Shanghai, China).

(3) Thermodynamic calculations

In order to investigate the corrosion processes of the specimens and understand the formation mechanisms of the composite spinel layers during the corrosion test, the phase evolution processes of the specimens M20 and

Table 1: Batch compositions of the specimens.

Ingredient (wt%)	M0/NM0	M5/NM5	M10/NM10	M20/NM20	M30/NM30
Light MgO	0	5	10	20	30
Fe_3O_4	100	95	90	80	70

NM30 in the electrolyte were simulated using the thermodynamic software FactSage 6.2 in combination with the databases of Fact53, SGTE and FToxid [22]. The equilibrium phases were predicted using the Equilib module, considering the following as possible phases: gas, slag or liquid and various solid solutions. The calculations were performed for a constant temperature of 900 °C and pressure of 1 atm, and selected 100 g mixed electrolyte as the original corrosion slag. Alpha was defined as the weight ratio of the specimens to the electrolyte, which corresponds to the corrosion distance [23]. When Alpha was 2, the calculation was performed with 100 g electrolyte and 200 g of the specimens.

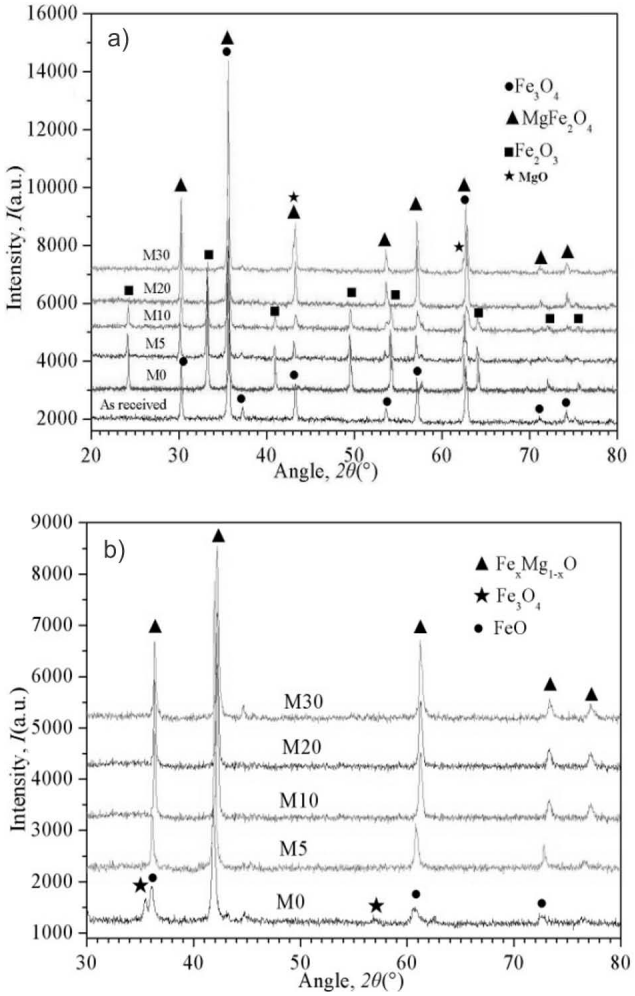

Fig. 2: The XRD patterns of the specimens after firing at 1400 °C in air (a) and N_2 (b).

III. Results

(1) Sintering process

The phase compositions of the specimens sintered at 1400 °C in air and nitrogenare shown in Figs. 2a and b, respectively. For the specimens sintered in air, it could be seen that the Fe_3O_4 phase disappeared completely in specimen M0 while Fe_2O_3 was generated after firing at 1400 °C [21] (Fig. 2a). The two phases, $MgFe_2O_4$ and Fe_2O_3, coexisted in specimens M5 and M10, indicating that the MgO reacted with some Fe_2O_3 to form $MgFe_2O_4$ spinel. Only $MgFe_2O_4$ spinel can be detected in specimen M20 because the mole ratio of MgO and Fe_2O_3 was 1:1. Besides $MgFe_2O_4$ phase, some residual MgO can be also found in specimen M30. As for the specimens sintered in nitrogen (Fig. 2b), most Fe_3O_4 phase in specimen NM0 was reduced to FeO. And in the MgO-containing specimens, all the Fe_3O_4 transformed into FeO phase, which subsequently reacted with MgO to form the $Fe_xMg_{1-x}O$ solid solution. The above observations were in agreement with the Fe-N-O (Fig. 1) and Mg-Fe-O phase equilibrium diagrams [24, 25].

The relative density of the specimens sintered in air and nitrogen is shown in Fig. 3. It can be seen that the relative density decreased for the specimens fired in both air and nitrogen when the MgO content was increased from 5 to 30 wt%. The theoretical calculations indicate that the formation of $MgFe_2O_4$ spinel phase based on the reaction of MgO with Fe_2O_3 is accompanied by 6.7 % volume expansion. Thus, the increase in MgO content was unfavorable for densification of the specimens prepared in air owing to the larger volume expansion. For the specimens prepared in nitrogen, the reduction in densification with the increase in MgO addition was mainly attributed to the fact that the melting point of $Fe_xMg_{1-x}O$ solid solution evidently increased with the increase in MgO content [26].

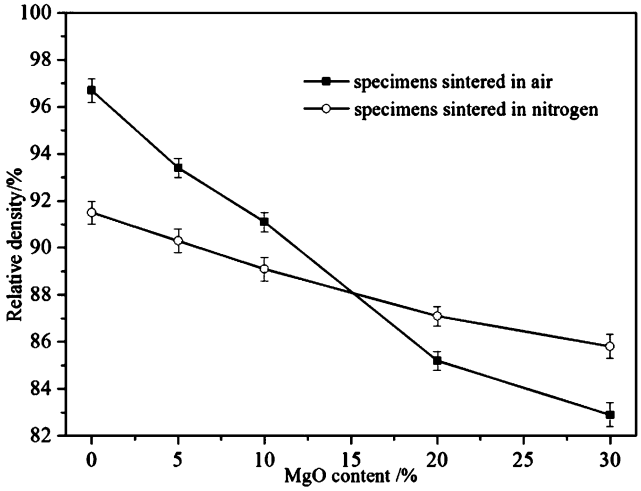

Fig. 3: The relative density of the cylindrical specimens sintered in air and nitrogen at 1400 °C.

(2) Corrosion test

After the corrosion test, the average thickness of the corrosion layer formed on specimens was measured from the SEM images of the specimen cross-section. The results for the specimens prepared in air and nitrogen are listed in Table 2 and Table 3, respectively. No obvious corrosion layer was formed on the specimens M0 and NM0. The corrosion layer thickness on the specimens M5, M10, M20 and M30 measured 170 μm, 160 μm, 90 μm and 120 μm, respectively. However, compared with the specimens prepared in air, the specimens prepared in nitrogen exhibited inferior corrosion resistance. The corrosion layer on specimens NM5, NM10, NM20 and NM30 measured 660 μm, 970 μm, 880 μm and 610 μm, respectively.

Table 2: Average thickness of corrosion layer of specimens fired at 1400 °C in air after test in molten electrolyte.

	M0	M5	M10	M20	M30
Corrosion layer thickness (μm)	–	170±4	160±4	90±3	120±3

Table 3: Average thickness of corrosion layer of specimens fired at 1400 °C in nitrogen after test in molten electrolyte.

	NM0	NM5	NM10	NM20	NM30
Corrosion layer thickness (μm)	–	660±4	970±5	880±5	610±4

After the corrosion test, no obvious corrosion phenomenon was observed on the specimens M0 and NM0 and only a slice of electrolyte penetrated into their surface (Fig. 4a and Fig. 6a), indicating that Fe_2O_3, FeO and Fe_3O_4 exhibited high chemical stability in molten electrolyte [15]. However, the pure FeO, Fe_3O_4 and Fe_2O_3 materials are not suitable for application as sidewalls since the dissolved iron impurity has a severely negative influence on the aluminum quality [27].

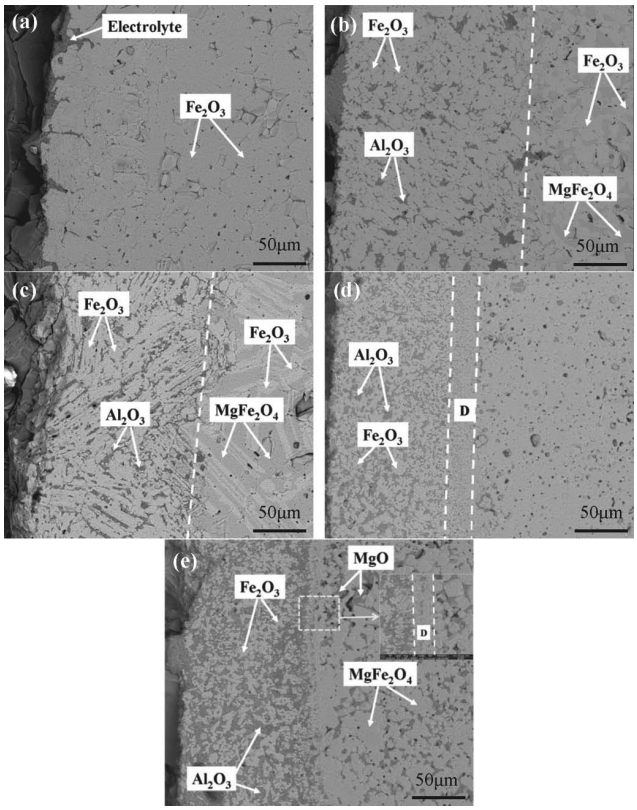

Fig. 4: Micrographs of the corroded specimens M0 (a), M5 (b), M10 (c), M20 (d) and M30 (e) prepared in air.

In fact, the corrosion process of the materials in the electrolyte is strongly related to their phase composition as well as densification [11, 28]. However, in the case of the prepared MgO-Fe_2O_3(FeO) specimens, the corrosion resistance appeared to be much more dependent on the phase composition than on the densification. For example, compared with the specimens prepared in air (Figs. 4b-e), much more serious corrosion occurred in the specimens prepared in nitrogen (Figs. 6b-d), indicating that the $Fe_xMg_{1-x}O$ phase had lower chemical stability than that of $MgFe_2O_4$ spinel phase in the electrolyte. Moreover, specimens M20 and NM30 exhibited the best corrosion resistance for the MgO-Fe_2O_3(FeO) specimens prepared in air and nitrogen respectively in spite of their relatively low densification.

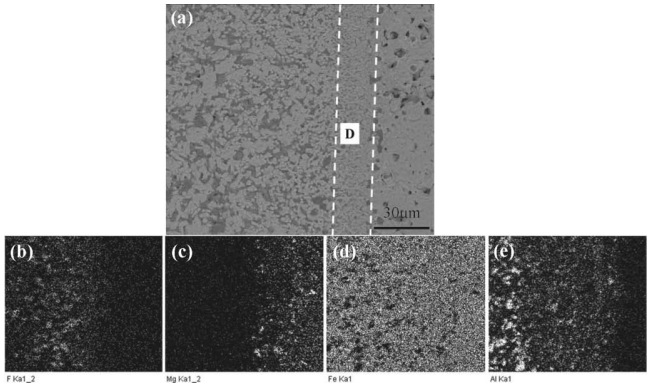

Fig. 5: Enlarged SEM image of corroded specimen M20 (a) and elemental maps of F(b), Mg (c), Fe (d) and Al (e).

In specimen M20, a distinctive white layer (D) of approximately 30 μm thickness (the area between the two lines marked on Fig. 4d) was formed between the corrosion layer and origin layer, and a thinner dense layer (about 10 μm) also appeared in M30 (Fig. 4e). The enlarged SEM image of the corroded specimen M20 (Fig. 5a) indicated that the distinctive layer consisted of very fine grains and it was much denser than the specimen itself. The elemental maps (Figs. 5b-e) showed that Mg was greatly depleted in the corrosion layer. No F and Al could be detected behind the dense ceramic layer, indicating that infiltration of the electrolyte was effectively inhibited. And Fe, Al and Mg concentrations were rather high in the dense ceramic layer, inferring that the ceramic layer was composed of composite spinel with a formula of $Mg(Al,Fe)_2O_4$. Based on the above observations, it can be deduced that the remarkably improved corrosion resistance of the specimen M20 could be attributed to the formation of the dense $Mg(Al,Fe)_2O_4$ composite spinel layer. Similarly, a white layer identified as $(Fe,Mg)Al_2O_4$ composite spinel was formed between the corrosion layer and origin layer for specimen NM30 (Fig. 6d). However, compared with the $Mg(Al,Fe)_2O_4$ layer in M20, the $(Fe,Mg)Al_2O_4$ layer in specimen NM30 was more fragmentary and looser. As a result, a relative thick corrosion layer was still formed in specimen NM30 although the $(Fe,Mg)Al_2O_4$ layer in the specimen inhibited the corrosion process to some extent.

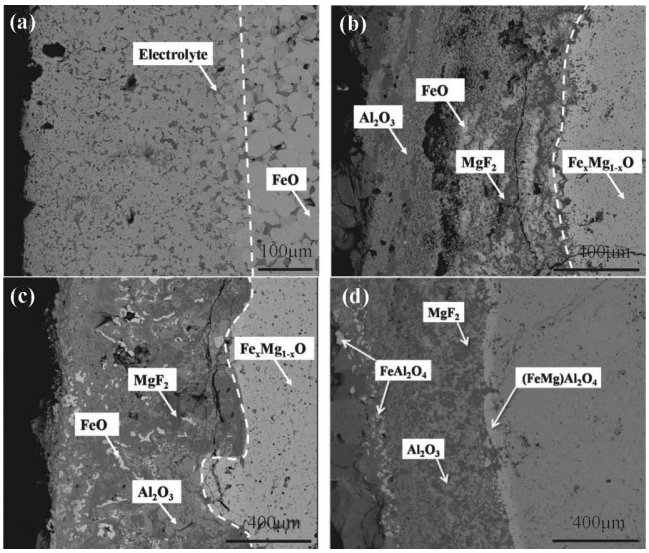

Fig. 6: Micrographs of the corroded specimens M0 (a), M10 (b), M20 (c) and M30 (d) prepared in nitrogen.

IV. Discussion

In order to investigate the corrosion processes of the specimens and understand the formation mechanisms of the composite spinel layers during the corrosion test, thermodynamic analysis was undertaken to simulate the phase evolution processes of specimens M20 and NM30 in the electrolyte, and the results are shown in Fig. 7. Fig. 7a shows the predicted phases for the system containing specimen M20 and electrolyte as a function of Alpha. When Alpha increases, the phase amounts of K_3AlF_6, AlF_3 and $Na_5Al_3F_{14}$ decrease continuously and drop sharply to zero when Alpha reaches about 1.4, 0.8 and 1.9 respectively, whereas Fe_2O_3, Al_2O_3 and some fluorides (MgF_2, $KMgF_3$ and $NaMgF_3$) occur simultaneously. The Al_2O_3 content increases with increasing Alpha from 0 to 2.0. However, thereafter it steadily decreases and disappears when Alpha is about 2.6. Correspondingly, a composite spinel is generated when the Alpha is 2.0 and its content increases successively after appearing. In combination with DES results (Figs. 5b-e) and thermodynamic calculations, the corrosion progresses of specimen M20 in electrolyte melts can be deduced as follows. During the corrosion test, after the interaction between the specimen and the adequate electrolyte, Fe_2O_3, Al_2O_3 and the fluorides (MgF_2, $KMgF_3$ and $NaMgF_3$) are produced via reactions (1) – (3). The dissolution of the fluorides into the molten electrolyte leads to the depletion of Mg element in the corrosion layer (Fig. 5b). With the increase in the corrosion distance (increase in Alpha for thermodynamic predictions), the Al_2O_3 formed in the corrosion layer reacts with the $MgFe_2O_4$ phase to generate $Mg(Al,Fe)_2O_4$ composite spinel (reaction (4)) layer deposited between the corrosion layer and the origin layer (Fig. 5a) [29]. After the test, only M20 and M30 had the $Mg(Al,Fe)_2O_4$ composite spinel layer for the specimens prepared in air, which demonstrated that the presence of high $MgFe_2O_4$ phase in the matrix was favorable for the formation of the composite spinel layer (reaction (4)).

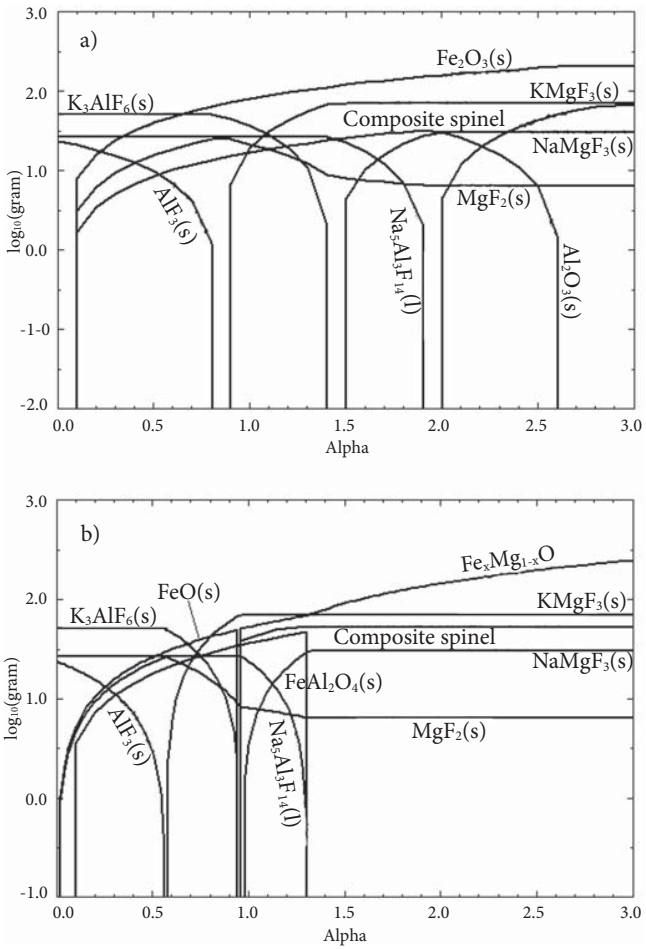

Fig. 7: Phase evolution of the specimen M20 (prepared in air) (a) and M30 (prepared in nitrogen) (b) in the electrolyte at 900 °C.

The phase evolutions for the system containing specimen NM30 and electrolyte with Alpha are given in Fig. 7b. As the Alpha value increases, unsurprisingly the K_3AlF_6, AlF_3 and $Na_5Al_3F_{14}$ contents decrease progressively, which is accompanied by the formation of FeO, $FeAl_2O_4$ and fluorides (MgF_2, $KMgF_3$ and $NaMgF_3$). However, the FeO and $FeAl_2O_4$ disappear abruptly when Alpha is 0.95 and 1.3, respectively. It is worth noting that as Alpha increases to 0.95, $Fe_xMg_{1-x}O$ and a composite spinel are generated simultaneously and the composite spinel increases gradually after appearing and remains constant when Alpha exceeds 1.3. The thermodynamic calculations indicated that in the first contact between the specimen and sufficient electrolyte, total dissolution of the $Fe_xMg_{1-x}O$ phase occurred owing to reaction (5), resulting in the formation of FeO, Al_2O_3 and MF_2 phases. Owing to the reaction of FeO and Al_2O_3 (reaction (6)), $FeAl_2O_4$ phase would be generated. And the presence of the $FeAl_2O_4$ grains at the interface between the electrolyte and corrosion layer (Fig. 6d) inferred that reaction (6) was more likely to occur between FeO and the Al_2O_3 that dissolved in the electrolyte [28, 30]. With increasing corrosion distance, the Al_2O_3 formed would react with $Fe_xMg_{1-x}O$ (reaction (7)) at a certain place to generate the $(Fe,Mg)Al_2O_4$ composite spinel layer (Fig. 6d). The higher Mg content in the $Fe_xMg_{1-x}O$ would result in the formation of more Al_2O_3 phase (reaction (5)) in the

corrosion layer, which would promote the formation of the $(Fe,Mg)Al_2O_4$ composite spinel layer (reaction (7)). Therefore, only specimen NM30 possessed a composite spinel layer (although fragmentary and loose) after the test.

According to the observation results of Yan *et al.* [1], the $Mg(Al,Fe)_2O_4$ and $(Fe,Mg)Al_2O_4$ spinel solution layers should possess relatively high chemical stability in the electrolyte owing to the reduced activities of the oxides in the spinel solution. Thus, the composite spinel layers formed improved the corrosion resistance of specimens M20, M30 and NM30. Furthermore, during the corrosion process, the formation of composite spinel layer was closely related to the crystallographic structure (phase composite) of compounds in the specimens. The formation of $Mg(Al,Fe)_2O_4$ spinel would result in a slight volume change owing to the same crystallographic structure of $MgFe_2O_4$ and $Mg(Al,Fe)_2O_4$ (Fd-3m) [9], while significant volume expansion would occur in the $(Fe,Mg)Al_2O_4$ spinel formation process since the crystallographic structure of $Fe_xMg_{1-x}O$ (Fm-3m) was different from $(Fe,Mg)Al_2O_4$ spinel (Fd-3m) [31]. As a result, the $(Fe,Mg)Al_2O_4$ spinel layer formed in specimen NM30 was much looser than the $Mg(Al,Fe)_2O_4$ layer in specimens M20 and M30, and specimens M20 and M30 exhibited much better corrosion resistance than that of specimen NM30.

$$3MgFe_2O_4(s) + 2AlF_3(s) = 3MgF_2(s) + Al_2O_3(s) + 3Fe_2O_3(s) \quad (1)$$

$$MgF_2(s) + NaF(s) = NaMgF_3(s) \quad (2)$$

$$MgF_2(s) + KF(s) = KMgF_3(s) \quad (3)$$

$$MgFe_2O_4(s) + xAl_2O_3(s) = Mg(Al,Fe)_2O_4(s) + xFe_2O_3(s) \quad (4)$$

$$2(1-x)AlF_3(s) + Fe_xMg_{1-x}O(s) = 3(1-x)MgF_2(s) + 3xFeO(s) + (1-x)\,Al_2O_3(s) \quad (5)$$

$$FeO(s) + Al_2O_3(s) = FeAl_2O_4(s) \quad (6)$$

$$Fe_xMg_{1-x}O(s) + Al_2O_3(s) = (Fe,Mg)Al_2O_4(s) \quad (7)$$

V. Conclusions

The following conclusions can be made on the basis of the sintering behavior of MgO-Fe_2O_3(FeO)materials and their corrosion test results in molten electrolyte:

(1) At high temperatures, the Fe_3O_4 phase is transformed into Fe_2O_3 in air, which in turn reacts with the MgO added to form the $MgFe_2O_4$ spinel. With the increase in the MgO addition, the densification of the specimens prepared in air decreases, mainly due to the larger volume expansion resulting from formation of more $MgFe_2O_4$ spinel. For the specimens prepared in nitrogen, most Fe_3O_4 phase was reduced to FeO in specimens without MgO while all the MgO-added specimens are composed of $Fe_xMg_{1-x}O$ solid solution only. The densification of the specimens reduced notably with the amount of MgOadded because of the improved melting point of the $Fe_xMg_{1-x}O$ solid solution.

(2) The corrosion tests show that corrosion layers are produced in all the MgO-added specimens while the corrosion process can be inhibited when a composite spinel layer is formed on the surface of the specimens during the test. Moreover, since the $MgFe_2O_4$ spinel phase had higher chemical stability than that of the $Fe_xMg_{1-x}O$ phase in the electrolyte and a protective composite spinel layer with dense structure can be formed more in specimens prepared in air, the specimens prepared in air generally exhibited much better corrosion resistance than that of the specimens prepared in nitrogen despite having the same starting material composition.

Acknowledgements

This project is financially supported by National Natural Science Fund of China (51202168) and the Natural Science Foundation of Hubei Province (2013CFA105 and ZRZ0348).

References

1 Yan, X.Y., Mukhlis, R.Z., Rhamdhani, M.A., Brooks, G.A.: Aluminate spinels as sidewall linings for aluminum smelters, *Light Met.*, 1085 – 1090, (2011).

2 Sonntag, A.: New R-SiC extends service life in kiln furniture, *Am. Ceram. Soc. Bull.*,**76**, [11], 51 – 54, (1997).

3 TaKahashi, K., Murase, H., Yoshida, S., Houjou, K., Ando, K., Saito, S.: Improvement of static fatigue strength of Si_3N_4/SiC crack-healed under cyclic stress, *J. Eur. Ceram. Soc.*, **25**, 1953 – 1959, (2005).

4 Ghanem, H., Gerhard, H., Popovska, N.: Paper derived SiC-Si_3N_4 ceramics for high temperature applications, *Ceram. Int.*, **35**, 1021 – 1026, (2009).

5 Gao, B.L., Wang, Z.W., Qiu, Z.X.: Corrosion tests and electrical resistivity measurement of SiC-Si_3N_4 refractory materials, *Light Met.*, 419 – 424, (2004).

6 Brooks, G., Cooksey, M., Wellwood, G.: Challenges in light metals production, *Miner. Process. Extr. Metall.*, **116**, [1], 25 – 33, (2007).

7 Mukhlis, R., Rhamdhani, M.A., Brooks, G.: Sidewall materials for Hall-Héroult process, *Light Met.*, 883 – 888, (2010).

8 Hang, E., Einarsrud, M., Grande, T.: Chemical stability of ceramic sidelinings in hall-heroult cells, *Light Met.*, 257 – 263, (2001).

9 Nightingale, S.A., Longbottom, R.J., Monaghan, B.J.: Corrosion of nickel ferrite refractory by Na_3AlF_6-AlF_3-CaF_2-Al_2O_3 bath, *J. Eur. Ceram. Soc.*, **33**, [13 – 14], 2761 – 2765, (2013).

10 Pawlek, R.P.: Inert anode: Research, development, and potential, *Light Met.*, 50 – 55, (2002).

11 Yan, X.Y., Pownceby, M.I., Brooks, G.: Corrosion behaviour of nickel ferrite-based ceramics for aluminium electrolysis cells, *Light Met.*, 909 – 913, (2007).

12 Sadoway, D.R.: Inert anodes for the Hall-Héroult cell: The ultimate materials challenge, *JOM*, **53**, [5], 34 – 35, (2001).

13 Downie, K.: $NiFe_2O_4$ as a sidewall material in Hall-Héroult cells, Wollongong, University of Wollongong, 2007.

14 Kvande, H.: Inert electrodes in aluminum electrolysis cells, *Light Met.*, 369 – 376, (1999).

15 Jentoftsen, T.E., Lorentsen, O.A., Dewing, E.W., Haarberg, G.M., Thonstad, J.: Solubility of some transition metal oxides in cryolite-alumina melts: Part I. Solubility of FeO, $FeAl_2O_4$, NiO, and $NiAl_2O_4$, *Metall. Mater. Trans. B*, **3**, 901 – 908, (2002).

16 Olsen, E., Thonstad, J.: Nickel ferrite as inert anodes in aluminum electrolysis: Part I: Material fabrication and preliminary testing, *J. Appl. Electrochem.*, **29**, [3], 293 – 299, (1999).

17 Berchmans, L.J., Selvan, R.K., Augustin, C.O.: Evaluation of Mg^{2+}-substituted $NiFe_2O_4$ as a green anode material, *Mater. Lett*., **58**, 1928 – 1933, (2004).

18 Xu, Y.B., Li, Y.W., Sang, S.B., Ren, B., Qing, Q.W., Yang, J.H.: Preparation of MgO-$NiFe_2O_4$-TiO_2 materials and their corrosion in Na_3AlF_6-AlF_3-K_3AlF_6 bath, *Ceram. Int*., **40**, [8], 13169 – 13177, (2014).

19 Liu, H.W., Liu, H.F.: Synthesis of nanosize quasispherical $MgFe_2O_4$ and study of electrochemical properties as anode of lithium ion batteries, *J. Electron. Mater*., **43**, [7], 2553 – 2558, (2014).

20 Wang, J., Feng, M., Zhang, H.J., Xu, X.F.: Catalytic decomposition of N_2O over Mg-Fe mixed oxides, *J. Fuel Chem. Technol.*, **42**, [12], 1464 – 1469, (2014).

21 Chen, J.H., Yu, L.Y., Sun, J.L., Li, Y., Xue, W.D.: Synthesis of hercynite by reaction sintering, *J. Eur. Ceram. Soc*., **31**, [3], 259 – 263, (2011).

22 Luz, A.P., Braulio, M.A.L., Martinez, A.G.T., Pandolfelli, V.C.: Thermodynamic simulation models for predicting Al_2O_3-MgO castable chemical corrosion, *Ceram. Int*., **37**, [8], 3109 – 3116, (2011).

23 Luz, A.P., Martinez, A.G.T., Braulio, M.A.L., Pandolfelli, V.C.: Thermodynamic evaluation of spinel containing refractory castables corrosion by secondary metallurgy slag, *Ceram. Int*., **37**, [4], 1191 – 1201, (2011).

24 Phillips.B., Szmiya.S., Muan.A.: Melting relations of magnesium oxide-iron oxide mixtures in air, *J. Am. Ceram. Soc*.,**44**, [4], 167 – 169, (1961).

25 Wu, P., Eriksson, G., Pelton, A.D., Blander, M.: Prediction of the thermodynamic properties and phase diagrams of silicate systems-evaluation of the FeO-MgO-SiO_2 system, *ISIJ International*, **33**, [1], 26 – 35, (1993).

26 Deraz, N.M., Abd-Elkader, O.H.: Investigation of magnesium ferrite spinel solid solution with iron-rich composition, *Int. J. Electrochem. Sc*., **8**, 9071 – 9081, (2013).

27 Sterten, Å., Solli, P.A., Skybakmoen, E.: Influence of electrolyte impurities on current efficiency in aluminium electrolysis cells, *J. Appl. Electrochem*., **28**, [8], 781 – 789, (1998).

28 Liu, B., Zhang, L., Zhou, K., Wang, H.: Electrical conductivity and molten salt corrosion behavior of spinel nickel ferrite, *Solid State Sci*., **13**, [8], 1483 – 1487, (2011).

29 Liu, G.P., Li, N., Yan, W., Gao, C.H., Zhou, W., Li, Y.Y.: Composition and structure of a composite spinel made from magnesia and hercynite, *J. Ceram. Process. Res*., **13**, [4], 480 – 485, (2012).

30 Liu, J.Y., Li, Z.Y., Tao, Y.Q., Zhang, D., Zhou, K.C.: Phase evolution of 17(Cu-10Ni)-($NiFe_2O_4$-10NiO) cermet inert anode during aluminum electrolysis, *T. Nonferr. Metal. Soc*., **21**, [3], 566 – 572, (2011).

31 Ghosh, C., Ghosh, A., Haldar, M.K.: Studies on densification, mechanical, micro-structural and structure-properties relationship of magnesium aluminate spinel refractory aggregates prepared from indian magnesite, *Mater. Charact*., **99**, 84 – 91, (2015).